

Multi-environment robotic locomotion through integrated median-paired and caudal fin propulsion

Jingshu Peng^{a,1}, Yuanhao Xie^b, Qifan Yang^b, Yongxia Jia^{b,c,*}, Weixi Huang^{b,*}, Guangming Xie^{d,*}

^aXingjian College, Tsinghua University, Beijing, 100084, China

^bDepartment of Engineering Mechanics, Tsinghua University, Beijing, 100084, China

^cNational Experimental Teaching Demonstration Center for Mechanics, Tsinghua University, Beijing, 100084, China

^dIntelligent Biomimetic Design Lab, College of engineering, Peking University, Beijing, 100871, China

Abstract

Amphibious robots, inspired by both aquatic and terrestrial animals, are crucial for enhancing the capabilities of robotics across diverse environments. This research introduces a median-paired fin, also known as undulating-fin, propulsion system, which reduces size and weight of the robot while enabling effective movement in various environments. Moreover, we present a design featuring a combined propulsion system that integrates undulating fins with dual caudal fins. Through fluid dynamics analyses and real-world experiments, we have confirmed that this combined propulsion enhanced performance of the robot, achieving higher swimming speeds compared to using a single propulsion. Additionally, at equivalent speeds, the combined propulsion exhibits the potential for enhanced energy efficiency, reducing energy consumption by 10.7% compared to the undulating-fin propulsion alone. This innovative design also enhances underwater maneuverability, facilitating a diverse range of linear and turning motion patterns.

Keywords: Amphibious Robot, Biomimetic Design, Combined-propulsion, Undulating Fin, Fluid Simulation

1. Introduction

Amphibious robots represent an advanced class of robotic platforms with the ability to operate effectively in various environments, transitioning seamlessly between land and water (Ren and Yu, 2021). These robots are designed to perform a variety of tasks, from detection to combat operations, in diverse settings such as land, coastal areas, and complex underwater environments. Their versatile capabilities make them valuable for both civilian and military applications (Bai et al., 2022).

Due to the distinct differences between terrestrial and underwater propulsion, the predominant approach involves integrating separate movement mechanisms within amphibious robots. Commonly, wheels (Alvarez et al., 2014; Consi et al., 2010, 2009) and legs (Ayers, 2004; Paulson, 2004) are utilized for land navigation, while propellers (Boxerbaum et al., 2005; Ma et al., 2022; Vogel et al., 2014), fins (Wang et al., 2009; Yi et al., 2015), and other mechanisms facilitate underwater propulsion. This has led to ongoing research aimed at developing a unified propulsion system that can reduce structural complexity and enhance system reliability. Biomimetic amphibious robots, inspired by natural organisms, particularly amphibians, offer a promising solution to this challenge (Guo et al., 2018b). Several biomimetic robots have been developed with unified drive mechanisms inspired by various animals, such as crabs (Greiner et al., 1996; Wang et al., 2017), cockroaches (Dey et al., 2013;

Zhang et al., 2016), snakes (Ohashi et al., 2010), turtles (Guo et al., 2018a, 2012; Han et al., 2011; Wu et al., 2022), lobsters (Shi et al., 2013), and frogs (Fan et al., 2017; Yang et al., 2024). Additionally, attempts have been made to create biomimetic amphibious robot based on stingray (Filardo et al., 2020; Xia et al., 2023), expanding the use of median-paired fins, also known as undulating fins, for land propulsion. The undulating fin motion, known for its high maneuverability and efficiency at low speeds, allows these robots to adapt to complex environments and tasks.

Existing stingray-inspired amphibious robots typically use a design where each fin ray is driven by its own servo (Xia et al., 2023). This makes the robots large, cumbersome, and energy-intensive, limiting their performance across different environments. We introduce a undulating-fin propulsion system in which a single servo controls the entire fin on each side. This design reduces the size and weight of the robot while still allowing it to have effective movement in both terrestrial and aquatic environments. We also developed a combined undulating-fin and caudal-fin propulsion system to enhance underwater swimming speed and maneuverability, with notable potential for energy savings. This design was evaluated through Particle Image Velocimetry (PIV) experiments, Computational Fluid Dynamics (CFD) simulations, and real-world tests, providing a more efficient and versatile propulsion solution for amphibious robots.

The paper is organized as follows. Section 2 outlines the design of the amphibious robot. Section 3 focuses on the locomotion analysis, where we develop a three-dimensional locomotion model, followed by a discussion on the implementation

*Corresponding author. E-mail address: yongxiajia@tsinghua.edu.cn (Yongxia Jia), hwx@tsinghua.edu.cn (Weixi Huang), xiegming@pku.edu.cn (Guangming Xie).

¹This is the first author footnote.

of locomotion. This section also explores flow dynamics, drawing insights from both PIV experiments and CFD simulations. Section 4 presents the experimental results, and Section 5 concludes the paper and discusses potential directions for future work.

2. Design of the Amphibious Robot

The design of the robot is systematically segmented into three major components: the main body, caudal-fin propulsion system, and undulating-fin propulsion system, as depicted in Fig. 1(a). In the following sections, we will provide a detailed description of design of each components.

2.1. Design of the Robot Main Body

The robot main body comprises the head and body of the robot. The robot has a flat body and a streamlined head to reduce drag. The Outer shell of head, made from a transparent material, houses an infrared obstacle avoidance module and a camera module. The electronics in robot head are connected to the battery and Arduino board through an aerial plug situated at the front of the body, as shown in Fig. 1(b). Noteworthy is the presence of two waterproof servo slots on each side of the head, each slot housing a waterproof servo controlling the undulating fins.

The body adopts a box-type design with a detachable sealing cover on top, allowing easy access to internal circuits for convenient debugging. To ensure waterproofing, we implemented a static seal with a 1 cm wide groove designed to fit a silicone gasket. The cover is securely fastened to the edge of the body using screws, providing an effective seal. As shown in Fig.1(e), the Arduino board, battery, and breadboard are neatly organized within the body. For added safety, the power switch is mounted externally above the body. Fig.1(d) displays the supporting structures on both sides of the box, which prevent bending and deformation of the rotating rod, ensuring the stable operation of the undulating-fin propulsion system.

2.2. Design of the Propulsion Systems

The caudal-fin propulsion system, inspired by the grouper, feature a flat, square shape to prevent interference between the two fins. The side-by-side caudal fins are connected to waterproof servos via servo brackets, with the servos mounted on a connecting plate fixed to the rear of the robot, as shown in Fig. 1(c).

The undulating-fin propulsion system is composed of three primary components: the rotating rod, the fin rays, and the fixed rod. The front end of the rotating rod connects to the waterproof servo, while the rear end is secured to the connecting plate via a bearing. The middle section of the rotating rod consists of seven segments, with adjacent segments linked by off-center circular rods that have a 3 mm radius, creating a 90° phase difference between each pair, as illustrated in Fig.2(a). The fin rays feature a forked structure, with one end connecting to the these off-center rods and the other end attached to the fin surface, as shown in Fig.2(b). A central hole allows the carbon fiber fixed

rod to pass through. The fixed rod also extends through the robot head and the connecting plate, enhancing the stability of the system. For land propulsion, the fixed and rotating rods are positioned at different heights, setting the surface of the undulating fins at a 14° angle from the horizontal. Additionally, four small rollers beneath the body provide additional support, reduce land resistance by converting sliding friction into rolling friction, thus enhancing speed, as depicted in Fig.2(c).

For the undulating fin, a 3 mm thick silicone sheet was selected after extensive material testing, providing an optimal balance between flexibility for undulation and rigidity for terrestrial locomotion. The fin features a two-dimensional fan-shaped surface that bends to generate a three-dimensional undulating motion. The design parameters of the undulating fin are illustrated in Fig.3(a). Point *A* represents the center of the rotating rod, point *B* denotes the center of the fixed rod, and point *C* is the outermost point of the undulating fin surface. The wave height, representing the vertical displacement of the outer fin surface relative to the fixed rod, is h . The eccentricity of the rotating rod is e , the distance between the fixed rod and the rotating rod is l , and the rotation angle of the eccentric rotating rod is θ . The inner arc diameter is denoted as R , the width as d , and the arc angle as α . The wavelength of the outer edge of the undulating fin is defined as $\lambda = R\alpha$. Using Eq. 1, the wave height h can be calculated as follows:

$$h(\theta) = \frac{ed \sin \theta}{\sqrt{e^2 + l^2 - 2el \cos \theta}} \quad (1)$$

The waveform of the outer fin surface, which is computed using $h(\theta)$, as shown in Fig. 3(b), closely resembles a sine wave. This suggests that we can directly apply the sinusoidal model introduced by Yin et al. (Yin et al., 2021) to fabricate our undulating fin. In this model, the length of the sinusoidal curve corresponds to the length of the outer arc and is defined as follows:

$$\int_0^{\frac{R\alpha}{4}} \sqrt{1 + \left(\frac{2\pi h}{R\alpha} \cos \left(\frac{4\pi}{R\alpha} z \right) \right)^2} dz = \frac{\alpha(R + d)}{4} \quad (2)$$

Using this equation and the structural parameters, the specific dimensions of the arc-shaped undulating fin can be determined. The final designed shape of the fin surface is shown in Fig. 3(c).

3. Locomotion Analysis of the robot

3.1. Three-Dimensional Locomotion Model

3.1.1. Coordinate System Setup

To analyze the kinematics and dynamics of the robot, a coordinate system is defined. This system comprises a fixed inertial coordinate system, denoted as $X_0-Y_0-Z_0$, and a robot solid-connected coordinate system, denoted as $X-Y-Z$. Given that the primary component of the robot model, excluding the caudal and undulating fins, is a rigid body, it serves as the reference base for the robot solid-connected coordinate system. The origin of these coordinates is set at the center of mass of the entire

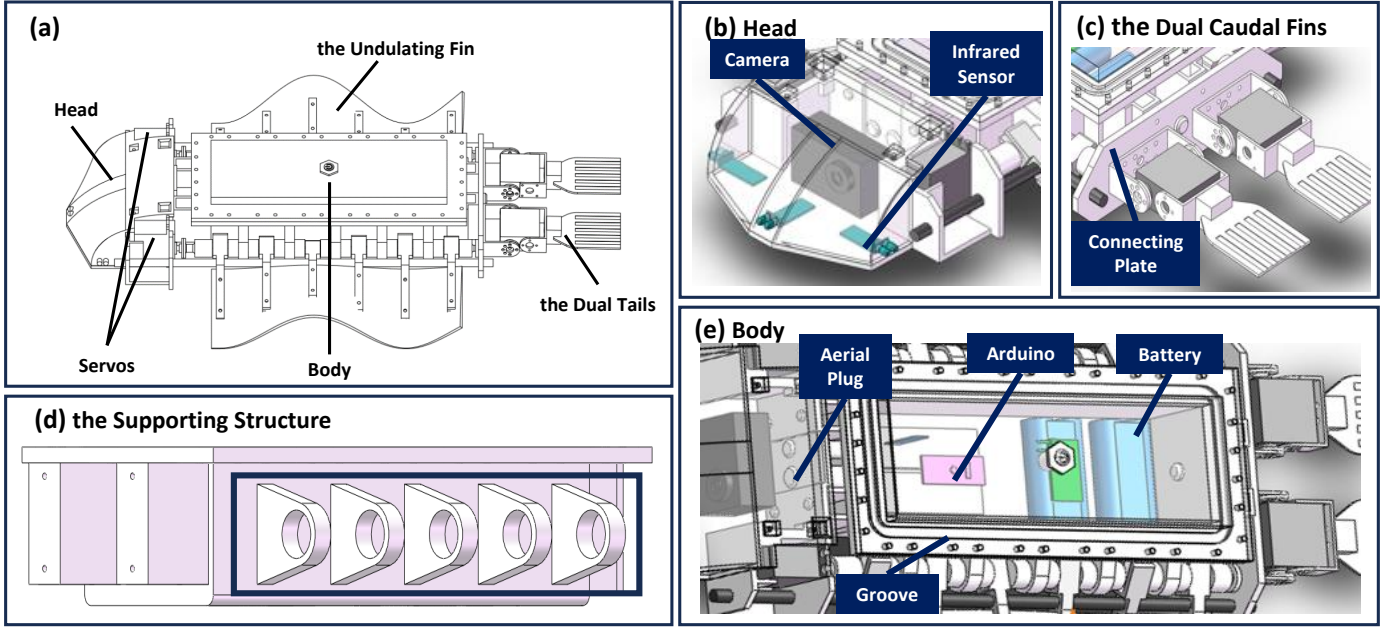


Fig. 1: (a) Overview of the robot design. (b) Detailed view of the head of the robot, showing sensory components and internal structure. (c) Model of the dual caudal fins with a detailed view of the connection between the body and caudal fins. (d) Illustration of the support structure providing stability for the undulating-fin propulsion system. (e) Model of the robot body, displaying the internal layout.

body. The orientation of the coordinate axes is established as follows: the positive Z -axis aligns with the front of the body, the positive X -axis corresponds to the top of the body, and the positive Y -axis is determined using the right-hand rule, as shown in Fig. 4(a).

3.1.2. Kinematic Analysis

The kinematics analysis on the robot has been performed according to the above solid-connected coordinate system. Within which the caudal fins flap and undulating fins fluctuate in place. Due to the symmetry of the body, it is adequate to focus on one side of the undulating fins and caudal fins.

The design of the undulating fin surface satisfies an approximate sinusoidal curve in the Z - X plane, as depicted in Fig. 4(b). The morphology of the fin surface should approximate the relationship outlined in Eq. 3 (i.e. the wave function of the fin surface):

$$\begin{cases} x(y, z, t) = A(y) \sin(\omega t + kz + \varphi_0) \\ f = \omega/2\pi \\ \lambda = 2\pi/k \end{cases} \quad (3)$$

where $x(y, z, t)$ denotes the position function of the undulating fin surface in three-dimensional space, and $A(y)$ is the amplitude control factor, which increases with the absolute value of y . The fin surface wave propagates along the negative direction of the Z -axis (towards the back of the robot), where f is the frequency of the fin surface wave, and λ is the wavelength.

The caudal fin can be treated as a rigid body rotating around a fixed axis, with its position determined by a single variable, the angle θ between the fin surface and the Y - Z plane, as illustrated in Fig. 4(c). Subsequently, the position of the caudal fin at each

moment can be obtained by integrating the angular velocity of the servo over time:

$$\theta(t) = \theta_0 + \int_0^t \omega(t) dt \quad (4)$$

where θ_0 represents the initial position of the caudal fin, and $\omega(t)$ is the function describing the rotational velocity.

3.1.3. Hydrodynamic Analysis

In the hydrodynamic analysis for the caudal-fin propulsion of the robot, the thrust force is derived from various aspects such as inertial force, leading-edge suction, trailing vortex, and caudal lift (Tong, 2000). In our study, we will focus specifically on inertial force and trailing vortex.

The propulsion of the robot is generated by the interaction of the undulating fins and the caudal fins with the water. During swimming, the undulating fins create a backward-propagating wave along the fish body, which propels the robot forward. This thrust is analogous to the inertial force previously discussed, as the change in fluid momentum induced by the fins results in forward thrust F . Theoretical models, such as Lighthill's elongated body theory (Sir James, 1975) and Tong's three-dimensional undulating plate theory (Sir James, 1975; Tong et al., 1991), indicate that undulation can produce forward motion when the wave speed c exceeds the swimming speed u . For the caudal fins, the propulsion force originates from the generation of reverse Kármán vortex streets, which produce reaction forces that drive the robot forward.

3.1.4. Dynamics Modeling

The robot consists of five primary components: the main body, dual undulating fins, and dual caudal fins. In the fol-

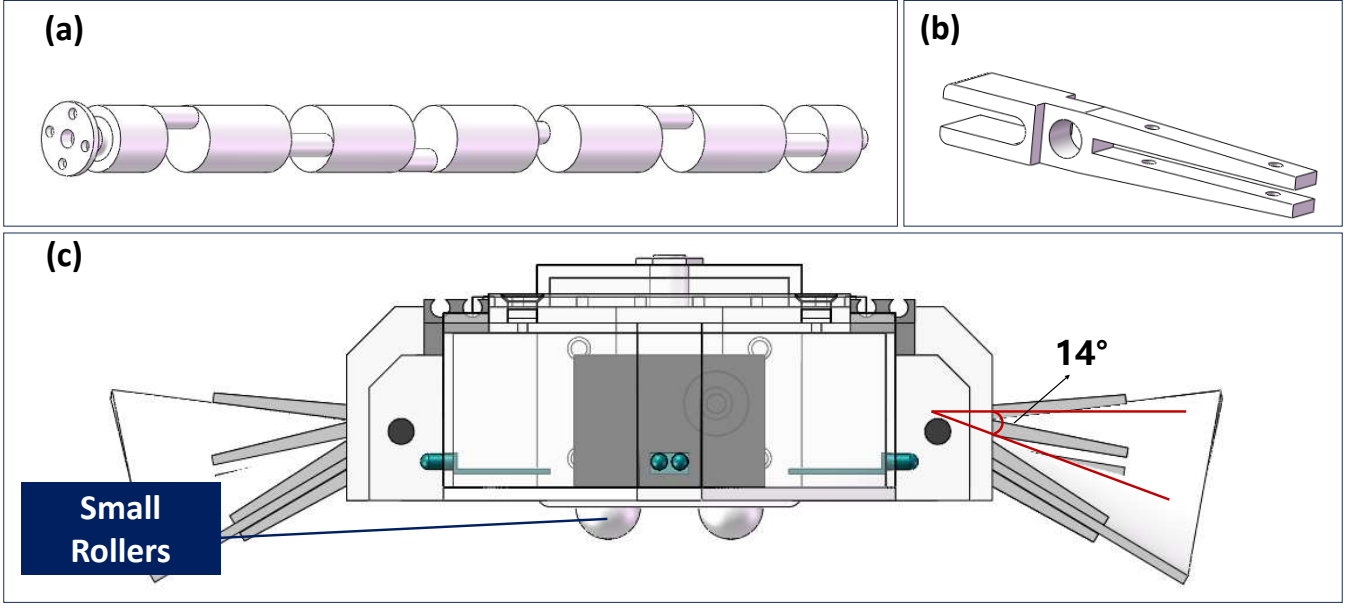


Fig. 2: (a) Diagram of the rotating rod structure driving the undulating fins. (b) Close-up of the fin rays, highlighting the forked design. (c) Front view of the body, showing the placement of the undulating fins relative to the body and the position of the four small rollers.

lowing analysis, we focus solely on the motion of the main body, while the other four components are simplified as a power source and resistance. However, when calculating the mass and rotational inertia of the robot, these components are included in the assessment. The subsequent discussion provides a rigid-body dynamics analysis of the main body.

Consider the mass of the main body as m_1 , the mass of a single undulating fin as m_2 , and the mass of a single caudal fin as m_3 . The positions of the center of mass for the main body, the overall center of mass for the two undulating fins, and the overall center of mass for the two caudal fins are denoted as \mathbf{r}_1 , \mathbf{r}_2 and \mathbf{r}_3 , respectively, in the fixed inertial coordinate system X_0 - Y_0 - Z_0 . The robot center of mass position can be determined using the following equation:

$$\mathbf{r}_c = \frac{\mathbf{r}_1 m_1 + 2\mathbf{r}_2 m_2 + 2\mathbf{r}_3 m_3}{m_1 + 2m_2 + 2m_3} \quad (5)$$

The forces acting on each part of the robot include: gravity of the main body \mathbf{G} , buoyancy of the main body \mathbf{F} , drag of the main body (both chordal and lateral) \mathbf{R} , normal force of the undulating fins (defined as the vector sum of gravity and buoyancy) \mathbf{P}_1 , normal force of the caudal fins \mathbf{P}_2 , net propulsive force of the undulating fins (defined as the vector sum of the propulsive force and the drag force) \mathbf{T}_1 , and net propulsive force of the caudal fins \mathbf{T}_2 . For a robot swimming horizontally in water, there exists a kinetic equation in a fixed inertial coordinate system, as shown in Eq. 6:

$$\begin{cases} \mathbf{F} = \mathbf{G} + \mathbf{P}_1 + \mathbf{P}_2 \\ (m_1 + 2m_2 + 2m_3) \ddot{\mathbf{r}}_c = \mathbf{T}_1 + \mathbf{T}_2 - \mathbf{R} \end{cases} \quad (6)$$

The second equation above can be written in component

form:

$$\begin{cases} \ddot{X}_C = 0 \\ (m_1 + 2m_2 + 2m_3) \ddot{Y}_C = T_{1y} + T_{2y} - R_y \\ (m_1 + 2m_2 + 2m_3) \ddot{Z}_C = T_{1z} + T_{2z} - R_z \end{cases} \quad (7)$$

3.2. Implementation of Locomotion

In water, the robot performs four distinct forward movement patterns for linear motion. The first pattern involves the dual caudal fins operate with a half-cycle phase difference, producing a steady forward thrust. The second pattern features the dual caudal fins moving synchronously, without any phase difference. The third pattern employs only the undulating fins, generating backward-propagating waves that push against the water to create forward thrust. Last, in the combined swimming mode, the undulating fins generate forward propulsion while the dual caudal fins operate half a cycle out of phase, enhancing thrust and increasing the linear speed of the robot. For backward movement, the undulating fins reverse their action, generating forward-propagating waves that propel the robot in the opposite direction. On land, only the undulating fin system is used for locomotion. During forward movement, the fins generate forward-propagating waves that create friction against the ground, enabling the robot to move forward. For backward movement, they generate backward-propagating waves, facilitating reverse motion.

For acceleration motion, as outlined in Eq.6 and Eq.7, the robot accelerates from a stationary state under the force of its propulsion systems. As the velocity increases, so does the resistance \mathbf{R} of body. Eventually, this resistance balances out with the thrust, enabling the robot to maintain a steady-state speed. When the propulsion stops, thrust diminishes, and the robot decelerates until it comes to a full stop. To expedite decelera-

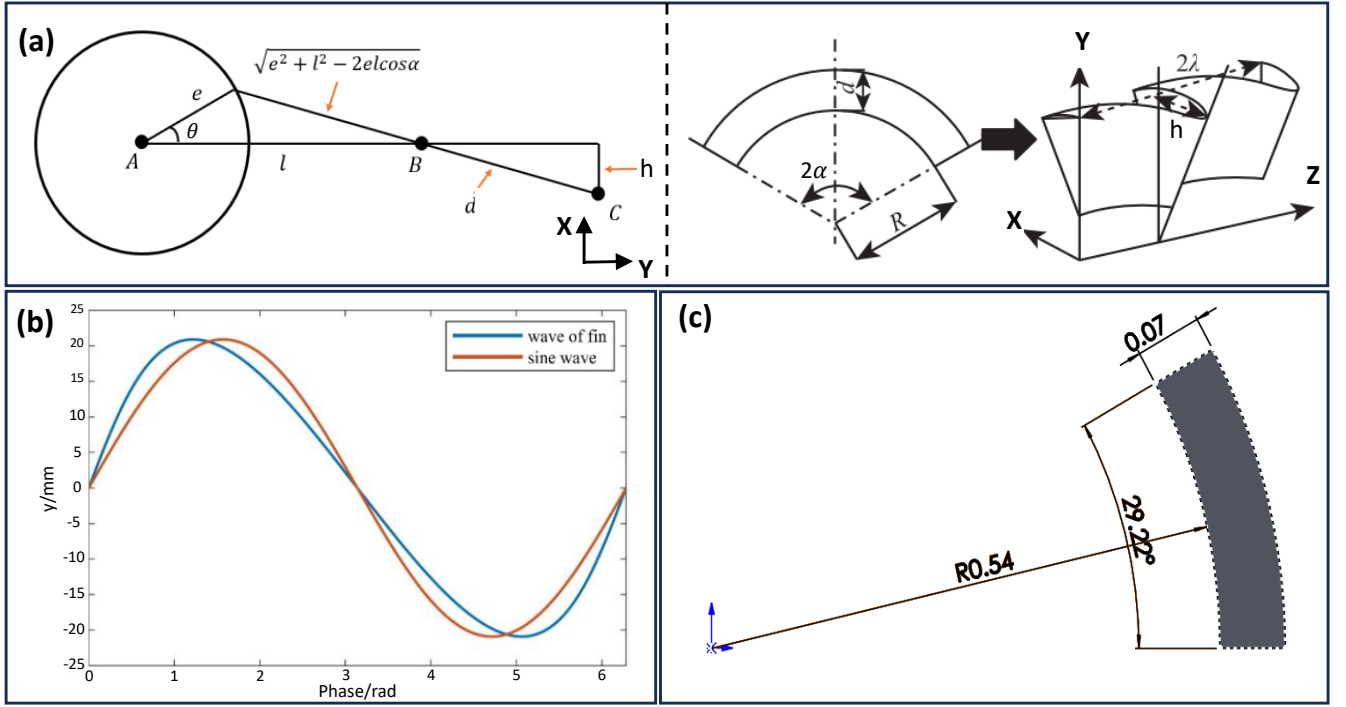


Fig. 3: (a) Schematic of undulating fin parameters. (b) Comparison of the actual wave shape h along the outer fin surface with sine wave, highlighting their similarity. (c) Final schematic of the undulating fin surface, showing the calculated parameters and refined shape.

tion in water, the undulating fins reverse direction to generate forward-directed surface waves, and the phase angle θ of the dual caudal fins are set to $-\pi/2$, increasing drag and enhancing braking.

For turning motions in water, asymmetrical motion of the undulating fins or caudal fins enables three distinct turning patterns. In the first pattern, the undulating-fin propulsion system enables the robot to turn in place by moving the fins in opposing directions; the turning radius can be adjusted by varying fin speeds. In the second pattern, the caudal-fin propulsion system, with a quarter-cycle phase difference, produces asymmetric thrust that generates torque for steering. In the third pattern, during linear propulsion with the undulating fins, positioning the dual caudal fins 180° apart functions as rudders, generating additional torque to facilitate turns. On land, the robot can also achieve turns by adjusting the undulating fins to move in opposite directions.

3.3. Flow Dynamics

3.3.1. PIV Experiment

We conducted PIV experiments for the caudal-fin swimming mode and the undulating-fin swimming mode. Given the symmetry of the robot about the Z-X plane, the undulating fin and caudal fin on one side were needed for the PIV experiments, as shown in Fig.5(a).

The experiments were performed in a low-turbulence water channel (Fig.5(b)), with a test section measuring 2 m in length, 0.4 m in width, and 0.5 m in height, allowing flow speeds to be adjusted up to 0.6 m/s. The incoming flow velocity was set at

$v_0 = 0.172$ m/s. The PIV system employed for the experiments (Fig.5(c)) included a high-speed CMOS camera (1024×1024 pixels @ 4 kHz), a 30 mJ pulsed laser (1 kHz), a data acquisition system, a data analysis software, and $10\ \mu\text{m}$ diameter tracer particles. During the experiments, the robot model was fixed within the test section of water channel. Flow field measurements were conducted using PIV to capture the velocity fields and flow patterns around the model.

3.3.2. CFD Simulation

For CFD simulation, a towing model is employed where the robot remains stationary while the fluid flows past it with a constant incoming velocity. During the swimming process, the undulating and caudal fins generate all the thrust and a small portion of the drag, whereas the main body contributes the majority of the drag. To focus on the thrust differences among various propulsion modes, the body is simplified to a rectangular box in the CFD simulations. However, the undulating fins and caudal fins are modeled with their precise dimensions and shapes, maintaining the relative positioning of all components. For the undulating-fin swimming mode, the caudal fins remain horizontal and stationary. In the caudal-fin swimming mode and the combined swimming mode, the dual caudal fins operate with a half-cycle phase difference, as shown in Fig. 5(d).

The robot model is positioned within a sufficiently large computational domain to ensure that boundary effects do not influence the flow around the model. A constant velocity condition is applied at the inlet, and a constant pressure condition is set at the outlet, while the boundaries of the domain and the surface of the model are treated as no-slip. The Reynolds-Averaged

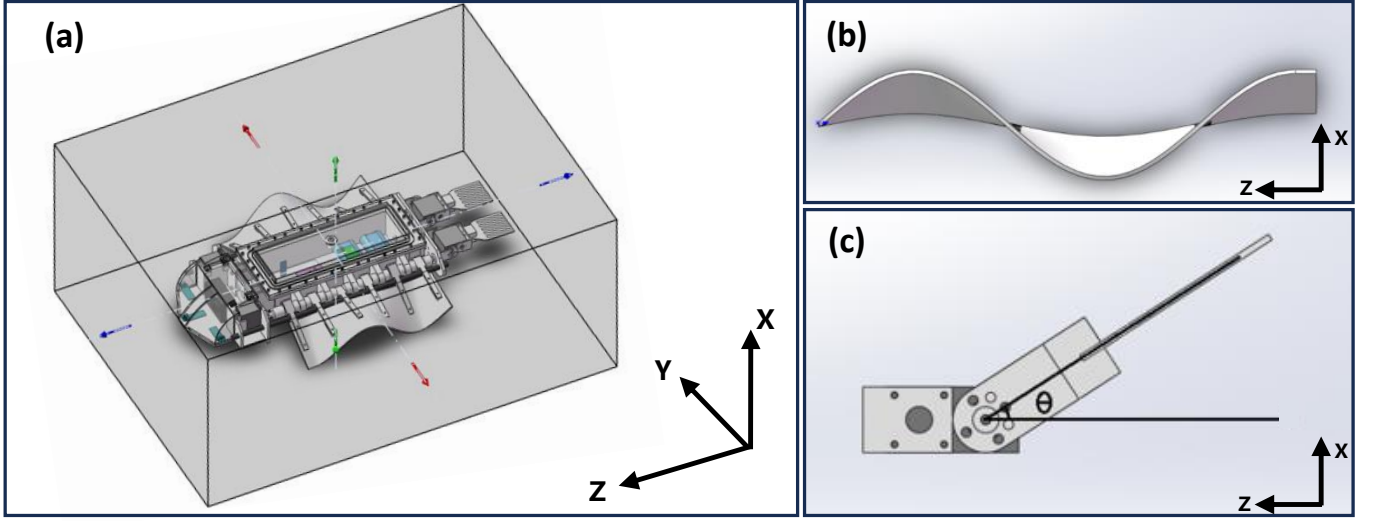


Fig. 4: (a) Schematic of the robot solid-connected coordinate system. (b) Side view of the undulating fin with a sinusoidal profile in the Z-X plane. (c) Side view of the caudal fin, rotating around a fixed axis at angle θ .

Navier-Stokes equations are employed to compute the velocity and pressure fields, with the Reynolds stresses determined using the $k - \omega$ SST model. The motions of the undulating and caudal fins are simulated using the dynamic mesh method, where the mesh deforms with the movement of the fins and is smoothed or remeshed as necessary at each time step.

Simulations are conducted for three swimming modes (undulating-fin, caudal-fin, and combined swimming modes) at the same incoming flow velocity of $u_0 = 0.172$ m/s. The undulating fins are set to a frequency of 1.9 Hz, while the caudal fins operate at a frequency of 0.8 Hz. The wavelength of the undulating fins is $\lambda = 18.4$ mm, and each fin contains one and a half wavelength.

3.3.3. PIV and Simulation Results

Fig. 5(e) presents the time histories of the drag force obtained from CFD simulation across three swimming modes. In the undulating-fin swimming mode, the drag force follows a sinusoidal pattern, with two periods occurring within each cycle of undulating motion. Due to the small amplitude of the undulating motion, the fins deform only slightly, resulting in relatively stable drag fluctuations. This leads to a steady swimming pattern in the undulating-fin swimming mode. In the caudal-fin swimming mode, the drag force exhibits four minima per cycle, corresponding to the moments when the caudal fins change direction and generate substantial thrust. In the combined swimming mode, the variation in drag force is similar to the trend observed in the dual caudal-fin swimming mode, both displaying four minima per cycle. Furthermore, we found that the average drag is lower than in the caudal-fin swimming mode, indicating a positive interaction between the undulating and caudal fins that enhances propulsion efficiency.

In the undulating-fin swimming mode, the velocity fields behind the fins, obtained from both PIV experiments and CFD simulations, are shown in Fig.5(f). Tip vortices shed from the

undulating fins generate low-speed streaks in the wake, clearly visible in the figure. This consistency between PIV experiments and CFD simulations demonstrates the reliability of using CFD for further analysis of flow structures. Fig.5(g) provides a visualization of these structures using the Q -criterion(Hunt et al., 1988). Across all three swimming modes, tip vortices are consistently observed on the fins. When the undulating fins are stationary, these vortices form at the wave crests and troughs, stretching along the flow direction and contributing to drag. Once undulation begins, the vortices shrink in size and become confined to the edges, reducing the low-pressure drag effect. Furthermore, trailing edge vortices from the caudal fins form a reverse Kármán vortex street, enhancing thrust. These observations suggest that the combination of undulating fins and caudal fins can enhance propulsion.

4. Experimental Testing and Validation

The specific parameters of the robot are shown in Tab. 1. The experiment on the underwater movement patterns of the bionic robot was conducted in a pool with a field of $3.5 \text{ m} \times 2 \text{ m} \times 0.6 \text{ m}$. A scale was positioned at the bottom of pool to measure the forward distance covered by the robot in the water. Adjacent to the pool, a video camera was placed for capturing and recording videos, facilitating subsequent data analysis. The experiments on the terrestrial movement patterns of the bionic robot were conducted on ceramic tiles.

The robot operates under five distinct propulsion modes: the undulating-fin swimming mode, the caudal-fin swimming mode, the combined swimming mode, the land-walking mode, and the water-land switching mode. The subsequent sections will delineate the processes and outcomes associated with each of these modes.

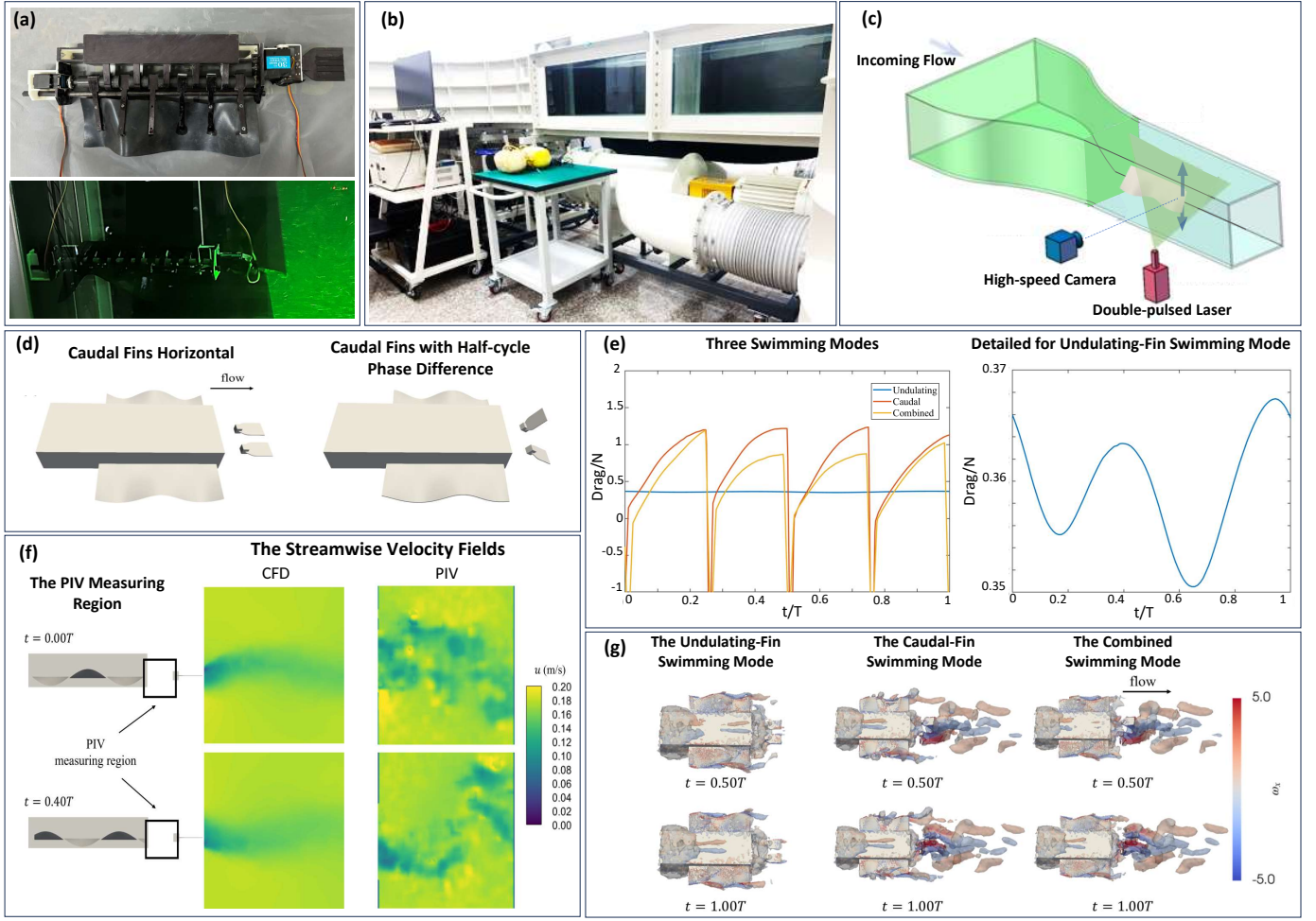


Fig. 5: (a) Setup of the robot model for PIV experiments. (b) Low-turbulence water channel used for the experiments. (c) Schematic of the PIV experimental design and measurement setup. (d) The robot model used in fluid dynamics simulations, showing different caudal fin positions. (e) Variation of total drag force over one cycle for three swimming modes, as obtained from CFD simulations. (f) Measurement region for the PIV experiments, along with streamwise velocity fields for the undulating-fin swimming mode obtained from both PIV experiments and CFD simulations. (g) Vortical structures of the robot across the three swimming modes, visualized using $Q = 1$ isosurfaces and colored by the streamwise vorticity ω_x .

4.1. Testing Methods and Procedures

The robot underwent waterproofing and weight adjustment processes prior to underwater testing. After these preparations, the robot was placed in a pool and controlled via software to perform various motion modes. Tests included linear and turning motions across three distinct propulsion modes: undulating-fin, caudal-fin, and combined swimming modes. Linear speed, turning speed, and turning radius were estimated through video analysis.

For the land movement test, the dual caudal fins were deactivated, and the robot performed forward, backward, and turning motions by adjusting the undulating frequency of the fins. Experiments also examined water-land transitions, using an inclined wooden board covered with a silicone sheet positioned by the pool. This setup allowed the robot to transition from land to water by controlling the switch between the land linear motion and the swimming linear motion.

4.2. Experimental Results Analysis

In the experimental swimming test, the efficiency of three propulsion modes was evaluated. The cost of transport (COT), introduced by Robert Baines et al. (Baines et al., 2022), quantifies the energy required to move a unit length of a robot. Taking into account the average input power of the robot $\overline{P_{in}(t)}$, the following equation was derived :

$$COT = \frac{\overline{P_{in}(t)}}{mg \cdot \overline{v_{bot}}} \quad (8)$$

where m is the mass of the robot, g is the local gravitational acceleration, and $\overline{v_{bot}}$ is the move average speed of the robot. We can calculate the power input of all servos via:

$$\overline{P_{in}(t)} = \sum_{i=1}^4 \overline{I_i(t)} V \quad (9)$$

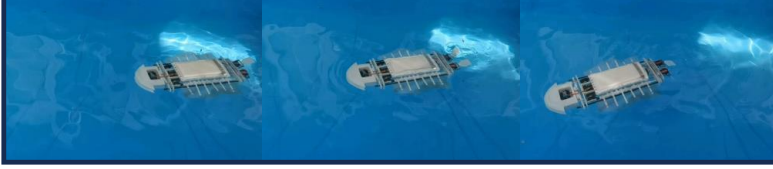
In the caudal-fin swimming mode, various tasks were carried out as shown in Fig.6(a). A quarter-cycle phase difference

(a) Caudal-Fin Swimming Mode

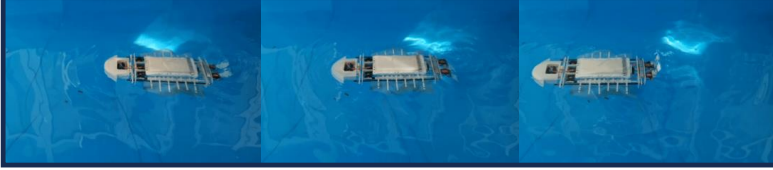
(1) Half-cycle phase difference



(2) Quarter-cycle phase difference



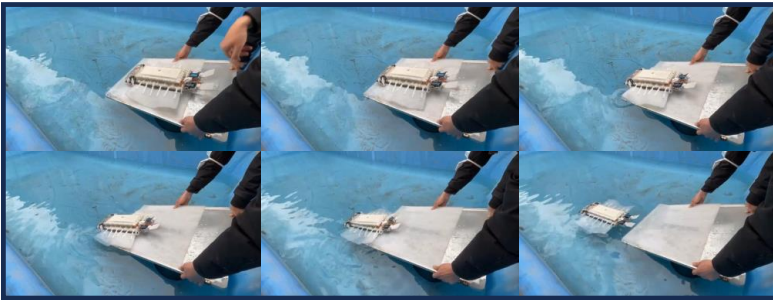
(3) Synchronous movement



(c) Combined Swimming Mode

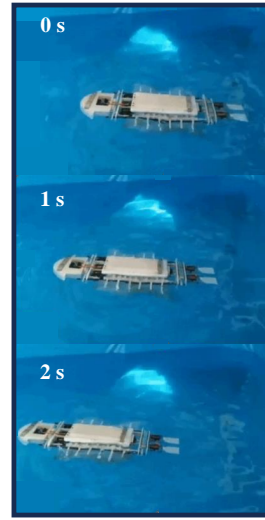


(e) Water-Land Switching Mode

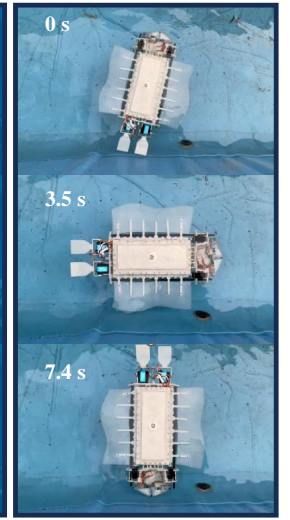


(b) Undulating-Fin Swimming Mode

Linear

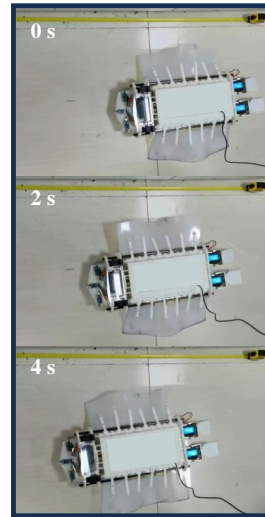


Turning



(d) Land-walking Mode

Linear



Turning



Fig. 6: (a) The robot performs a variety of movements by adjusting the phase difference between the dual caudal fins. (b) Linear and turning motions in the undulating-fin swimming mode. (c) Linear motion in the combined swimming mode. (d) Linear and turning motions in the land-walking mode. (e) Transition between water and land locomotion.

between the dual caudal fins, enabled smooth steering and produced a turning radius of approximately 4.6 m. The performance of the dual caudal fins was comparable during both synchronous movement and movement with a half-cycle phase difference. However, the synchronous movement exhibited some dorsal-ventral oscillation. When the fins moved with a half-cycle phase difference, the robot achieved a steady linear velocity of 0.05 m/s, with an average power output of 7.35 W, yielding a COT value of 5.61.

The undulating-fin swimming mode, shown in Fig.6(b), achieved linear speeds of 0.08 m/s, 0.09 m/s, and 0.10 m/s, with average power consumption values of 5.77 W, 6.78 W, and 7.98 W, respectively, and corresponding COT values of 2.75, 2.88, and 3.05. Notably, the minimal turning radius was approxi-

mately 0.301 m, highlighting its superior in-place turning capability, with a turning speed of 23.08°s^{-1} .

In the combined swimming mode, shown in Fig.6(c), the undulating fin frequency was set to the same as in the undulating-fin mode at a speed of 0.10 m/s, while the caudal fin frequency was kept the same as in the caudal-fin mode. Under these conditions, the robot achieved an increased forward speed of approximately 0.14 m/s, with an average power consumption of 11.92 W, resulting in a COT value of 3.25.

Additionally, experiments were conducted to assess both the terrestrial pivoting speed and linear motion of the biomimetic robot, as shown in Fig.6(d). The robot also demonstrated seamless transitions between underwater and terrestrial locomotion, as depicted in Fig.6(e). All results are summarized in Tab.2.

Table 1: Prototype Parameters of the Robot

Parameters	Unit	Value (s)
Body Length	mm	602
Overall Width	mm	413
Body Height	mm	95
Total Weight	kg	2.67
Torque of Caudal Fins' Servo	kg-cm	30
Torque of Undulating Fins' Servo	kg-cm	40
Capacity of Battery	mAh	1500
Battery Voltage	V	7.4
Robot Endurance	min	55
Remote Control Distance (Bluetooth)	m	3

Table 2: Experimental results of three swimming mode

Mode	Turning Radius (m)	Turning Speed ($^{\circ}\text{s}^{-1}$)	Linear Speed (m/s)	COT
The Causal-Fin Swimming Mode	4.6	-	0.05	5.61
The Undulating-Fin Swimming Mode	0.301	23.08	0.08 0.09 0.10	2.75 2.88 3.05
The Combined Swimming Mode	0.301	23.08	0.14	3.25

The experimental results indicate that at the same propulsion frequency, the combined swimming mode achieves a speed 40% higher than the undulating-fin swimming mode. Additionally, a robust linear relationship ($R^2 = 0.9941$) was observed between the speed of the undulating-fin swimming mode and its corresponding COT. Based on this, it can be calculated that when the speed of the undulating-fin swimming mode reaches 0.14 m/s, the COT will be 3.64. Therefore, at equivalent speeds, the combined swimming mode exhibits superior energy efficiency, consuming 10.7% less energy than the undulating-fin swimming mode. In conclusion, integrating undulating fins with dual caudal fins results in a smaller turning radius, faster speed, and the potential for enhanced energy efficiency.

5. Conclusions

This work introduces a undulating-fin propulsion system in which a single servo controls the entire fin on each side, enabling efficient motion in various environments while reducing size and weight of the robot. Our robot also features propulsion systems that combines undulating fins with dual caudal fins. Through PIV experiments, CFD simulations, and real-world tests, we demonstrate that the combined swimming mode achieves higher efficiency compared to using either the caudal-fin or undulating-fin swimming modes alone. Furthermore, a series of swimming experiments reveal that the integration of these two propulsion systems offers notable potential for energy savings, as measured by COT.

Our findings also indicate that the combined propulsion system facilitates a wide range of movement patterns. Underwater, the robot can generate propulsion for linear swimming using the undulating fins, the dual caudal fins, or a combination of both systems. For turning movements, the robot can achieve turns through asymmetric movements of the undulating and dual caudal fins or by employing the caudal fins as rudders. Additionally, the robot can perform both linear and turning motion on land, smoothly transitioning between aquatic and terrestrial environments. This research represents progress in the design and performance of amphibious robots.

In future work, we plan to refine the body structure and propulsion mechanisms through fluid simulations, flow visualization, and PIV. This will deepen our understanding of the physical mechanisms affecting the efficiency and speed of the combined propulsion system. Based on this research, we can further enhance the motion performance of the robot by leveraging the strengths of both propulsion systems.

Acknowledgement

The authors wish to acknowledge and thank Limu Wang, Xijie Mei, and Xinyu Tang for their invaluable assistance in the design and simulation of the robot throughout this project. Their expertise and support have been instrumental in the successful completion of this work.

This work was supported by the National Natural Science Foundation of China under Grant Nos. 12272008, 12425206, 92252204 and 12272206.

References

- Alvarez, J., Bertaska, I.R., von Ellenrieder, K., 2014. Nonlinear Control of an Unmanned Amphibious Vehicle, in: ASME 2013 Dynamic Systems and Control Conference. URL: <https://dx.doi.org/10.1115/DSCC2013-4039>.
- Ayers, J., 2004. Underwater walking. *Arthropod Structure & Development* 33, 347–360. URL: <https://www.sciencedirect.com/science/article/pii/S1467803904000362>.
- Bai, X.j., Shang, J.z., Luo, Z.r., Jiang, T., Yin, Q., 2022. Development of amphibious biomimetic robots. *J. Zhejiang Univ. Sci. A* 23, 157–187. URL: <https://doi.org/10.1631/jzus.A2100137>.
- Baines, R., Patiballa, S.K., Booth, J., Ramirez, L., Sipple, T., Garcia, A., Fish, F., Kramer-Bottiglio, R., 2022. Multi-environment robotic transitions through adaptive morphogenesis. *Nature* 610, 283–289. URL: <https://www.nature.com/articles/s41586-022-05188-w>.
- Boxerbaum, A., Werk, P., Quinn, R., Vaidyanathan, R., 2005. Design of an autonomous amphibious robot for surf zone operation: part i mechanical design for multi-mode mobility, in: *Proceedings, 2005 IEEE/ASME International Conference on Advanced Intelligent Mechatronics.*, pp. 1459–1464. URL: <https://ieeexplore.ieee.org/abstract/document/1511216>.
- Consi, T., Bingham, S., Chepp, J., Erdmann, T.R., Mehrotra, A., Ringstad, J., Zhao, B., 2010. Amphibious robots as rapidly deployable near-shore observatories, in: *OCEANS 2010 MTS/IEEE SEATTLE*, pp. 1–6. URL: <https://ieeexplore.ieee.org/abstract/document/5664106>.
- Consi, T.R., Ardaugh, B.R., Erdmann, T.R., Matsen, M., Peterson, M., Ringstad, J., Vechart, A., Verink, C., 2009. An amphibious robot for surf zone science and environmental monitoring, in: *OCEANS 2009*, pp. 1–7. URL: <https://ieeexplore.ieee.org/abstract/document/5422082>.

- Dey, B.B., Manjanna, S., Dudek, G., 2013. Ninja legs: Amphibious one degree of freedom robotic legs, in: 2013 IEEE/RSJ International Conference on Intelligent Robots and Systems, pp. 5622–5628. URL: <https://ieeexplore.ieee.org/abstract/document/6697171>.
- Fan, J.Z., Zhang, W., Kong, P.C., Cai, H.G., Liu, G.F., 2017. Design and Dynamic Model of a Frog-inspired Swimming Robot Powered by Pneumatic Muscles. *Chin. J. Mech. Eng.* 30, 1123–1132. URL: <https://doi.org/10.1007/s10033-017-0182-5>.
- Filardo, B.P., Zimmerman, D.S., Weaker, M.I., 2020. Vehicle with Traveling Wave Thrust Module Apparatuses, Methods and Systems. URL: <https://www.freepatentsonline.com/y2020/0149555.html>.
- Greiner, H., Shectman, A., Won, C., Elsley, R., Beith, P., 1996. Autonomous legged underwater vehicles for near land warfare, in: Proceedings of Symposium on Autonomous Underwater Vehicle Technology, pp. 41–48. URL: <https://ieeexplore.ieee.org/abstract/document/532399>.
- Guo, S., He, Y., Shi, L., Pan, S., Xiao, R., Tang, K., Guo, P., 2018a. Modeling and experimental evaluation of an improved amphibious robot with compact structure. *Robotics and Computer-Integrated Manufacturing* 51, 37–52. URL: <https://www.sciencedirect.com/science/article/pii/S0736584516300874>.
- Guo, S., Mao, S., Shi, L., Li, M., 2012. Development of an amphibious mother spherical robot used as the carrier for underwater micro-robots, in: 2012 ICME International Conference on Complex Medical Engineering (CME), pp. 758–762. URL: <https://ieeexplore.ieee.org/document/6275640>.
- Guo, Z., Li, T., Wang, M., 2018b. A Survey on Amphibious Robots, in: 2018 37th Chinese Control Conference (CCC), pp. 5299–5304. URL: <https://ieeexplore.ieee.org/abstract/document/8483367>.
- Han, B., Luo, X., Wang, X., Chen, X., 2011. Mechanism Design and Gait Experiment of an Amphibian Robotic Turtle. *Advanced Robotics* 25, 2083–2097. URL: <https://doi.org/10.1163/016918611X590300>.
- Hunt, J.C.R., Wray, A.A., Moin, P., 1988. Eddies, streams, and convergence zones in turbulent flows. center for turbulence research URL: <https://ntrs.nasa.gov/citations/19890015184>.
- Ma, X., Wang, G., Liu, K., 2022. Design and Optimization of a Multimode Amphibious Robot With Propeller-Leg. *IEEE Transactions on Robotics* 38, 3807–3820. URL: <https://ieeexplore.ieee.org/abstract/document/9803879>.
- Ohashi, T., Yamada, H., Hirose, S., 2010. Loop forming snake-like robot ACM-R7 and its Serpenoid Oval control, in: 2010 IEEE/RSJ International Conference on Intelligent Robots and Systems, pp. 413–418. URL: <https://ieeexplore.ieee.org/document/5651467?arnumber=5651467>.
- Paulson, L., 2004. Biomimetic robots. *Computer* 37, 48–53. URL: <https://ieeexplore.ieee.org/abstract/document/1333004>.
- Ren, K., Yu, J., 2021. Research status of bionic amphibious robots: A review. *Ocean Engineering* 227, 108862. URL: <https://www.sciencedirect.com/science/article/pii/S0029801821002973>.
- Shi, L., Guo, S., Mao, S., Li, M., Asaka, K., 2013. Development of a Lobster-Inspired Underwater Microrobot. *International Journal of Advanced Robotic Systems* 10, 44. URL: <https://doi.org/10.5772/54868>.
- Sir James, L., 1975. Mathematical biofluidynamics. SIAM.
- Tong, B., 2000. Propulsion mechanism of wave-like swimming in fishes. *Mechanics and Practice* 22, 69–74. [in Chinese].
- Tong, B., Zhuang, L., Cheng, J., 1991. Hydrodynamic study of fish wave-swing propulsion. *Mechanics and Practice* 13, 17–26. [in Chinese].
- Vogel, A.R., Kaipa, K.N., Krummel, G.M., Bruck, H.A., Gupta, S.K., 2014. Design of a compliance assisted quadrupedal amphibious robot, in: 2014 IEEE International Conference on Robotics and Automation (ICRA), pp. 2378–2383. URL: <https://ieeexplore.ieee.org/abstract/document/6907189>.
- Wang, G., Chen, X., Yang, S., Jia, P., Yan, X., Xie, J., 2017. Subsea crab bounding gait of leg-paddle hybrid driven shoal crablike robot. *Mechatronics* 48, 1–11. URL: <https://www.sciencedirect.com/science/article/pii/S095741581730140X>.
- Wang, W., Yu, J., Ding, R., Tan, M., 2009. Bio-inspired design and realization of a novel multimode amphibious robot, in: 2009 IEEE International Conference on Automation and Logistics, pp. 140–145. URL: <https://ieeexplore.ieee.org/abstract/document/5262958>.
- Wu, M., Xu, X., Zhao, Q., Afridi, W.H., Hou, N., Afridi, R.H., Zheng, X., Wang, C., Xie, G., 2022. A Fully 3D-Printed Tortoise-Inspired Soft Robot with Terrains-Adaptive and Amphibious Landing Capabilities. *Advanced Materials Technologies* 7, 2200536. URL: <https://onlinelibrary.wiley.com/doi/abs/10.1002/admt.202200536>.
- Xia, M., Wang, H., Yin, Q., Shang, J., Luo, Z., Zhu, Q., 2023. Design and Mechanics of a Composite Wave-driven Soft Robotic Fin for Biomimetic Amphibious Robot. *J Bionic Eng* 20, 934–952. URL: <https://doi.org/10.1007/s42235-022-00328-4>.
- Yang, Y., Xie, Y., Liu, J., Li, Y., Chen, F., 2024. 3D-Printed Origami Actuators for a Multianimal-Inspired Soft Robot with Amphibious Locomotion and Tongue Hunting. *Soft Robotics* URL: <https://www.liebertpub.com/doi/full/10.1089/soro.2023.0079>.
- Yi, Y., Geng, Z., Jianqing, Z., Siyuan, C., Mengyin, F., 2015. Design, modeling and control of a novel amphibious robot with dual-swing-legs propulsion mechanism, in: 2015 IEEE/RSJ International Conference on Intelligent Robots and Systems (IROS), pp. 559–566. URL: <https://ieeexplore.ieee.org/abstract/document/7353427>.
- Yin, Q., Shang, J., Jiang, T., Bai, X., Wang, H., Luo, Z., 2021. Fin surface structure design and motion simulation of flexible undulating fin amphibious robot. *Journal of Engineering Thermophysics* 42, 2954–2959. [in Chinese].
- Zhang, S., Zhou, Y., Xu, M., Liang, X., Liu, J., Yang, J., 2016. AmphiHex-I: Locomotory Performance in Amphibious Environments With Specially Designed Transformable Flipper Legs. *IEEE/ASME Transactions on Mechatronics* 21, 1720–1731. URL: <https://ieeexplore.ieee.org/document/7296639>.